CrossMark

ORIGINAL ARTICLE

Study on a bidirectional reflectance distribution function inversion model based on HJ-1 CCD imagery

Qingyan Meng[1] · Yunxiao Sun[1,2] · Xiaojuan Xue[1,2] · Xingfa Gu[1] · Rumiana Vatseva[4] · Jia-hui Zhang[1,2] · Tamas Jancso[3]

Abstract The surface bidirectional reflectance distribution function (BRDF) is an important factor in depicting the bidirectional reflectance characteristics of the land surface. In this study, BRDF is first inversed using a semiempirical, kernel-driven Algorithm for Model Bidirectional Reflectance Anisotropies of the Land Surface (Ambrals) model based on 4-day charge-coupled device (CCD) data from the HJ-1B satellite under clear sky conditions. Then, according to application needs, the inversion results of different angles are unified to the same observation angle to realize the radiometric normalization of BRDF at different viewing and incident directions. Finally, the inversed BRDF is compared with the measured BRDF in the principle plane and perpendicular plane of the Sun, respectively. The results show that: (1) The inversed BRDF based on the kernel-driven model is in good agreement with the measured BRDF. (2) The vegetation bidirectional reflectance in a backward scattering direction is higher than that in a forward scattering direction in the principle plane of the Sun. There is also a "hot spot" in the backward scattering direction. Additionally, the forward bidirectional reflectance is symmetrical relative to the backward one in the perpendicular plane of the Sun. (3) The geometric optical effect is more apparent in the visible bands of HJ-1B CCD, while the volume scattering effect is more significant in the near-infrared band. The Ambrals model and the procedures used in this study are effective and adapt to the characteristics of HJ-1B/CCD images. Therefore, our findings could advance the applications of the HJ-1 satellite and the development of quantitative remote sensing.

Keywords HJ-1B/CCD · Atmospheric correction · 6S model · Ambrals model · Directional reflectance

Introduction

Due to the complexity of three-dimensional geometries and spectral differences in surfaces, remote sensing data obtained under different viewing directions and incident directions show obvious anisotropic properties. This creates difficulties in comparing remote sensing data acquired at different times. The land surface bidirectional reflectance distribution function (BRDF) is a function to study the anisotropic reflectance characteristics of surface features. It is one of the most important parameters to characterize the Earth's radiative regime and its subsequent impact on biospheric and climatic processes (Dickinson 1995; Lofgren 1995; Zhang et al. 1995). Accurate inversion of BRDF is significant for many remote sensing applications. Recently, studying BRDF has become increasingly important for the development of medium-resolution and multi-angular remote sensing in Earth

✉ Qingyan Meng
  mengqy@radi.ac.cn

✉ Yunxiao Sun
  sunyx@radi.ac.cn

✉ Xiaojuan Xue
  xxj.0923@163.com

[1] Institute of Remote Sensing and Digital Earth, Chinese Academy of Sciences, Beijing 100101, China

[2] University of Chinese Academy of Sciences, Beijing 100049, China

[3] Department of Geography, National Institute of Geophysics, Geodesy and Geography, Bulgarian Academy of Sciences, Sofia, Bulgaria

[4] Alba Regia Technical Faculty, Obuda University, Budai ut 45, Szekesfehervar 8000, Hungary

observation systems. BRDF enables the comparison of remote sensing reversion results in varying geometric conditions. It further allows for the extraction of surface physical parameters and critical conditions of the Earth–atmosphere system. Nicodemus defined the BRDF precisely in the 1970s. However, mechanistic research on BRDF was not conducted systematically until the 1980s (Liu and Fan 2008).

To better understand the bidirectional reflectance process, scholars developed a series of theoretical models, including statistical, physical, and semiempirical models. The statistical models are relatively simple and practical, but lack theoretical and logical relationships between parameters. Physical models are theory based, but sometimes integrate too many assumptions and negligible or non-primary factors. Semiempirical models were developed to integrate the advantages of both statistical and physics-based models. Representative semiempirical models include both linear Kernel-driven model (Roujean et al. 1992; Wanner et al. 1995) and nonlinear models (Rahman et al. 1993).

Recent studies on radiometric normalization of BRDF are based primarily on advanced very high-resolution radiometer (AVHRR), multi-angle imaging spectroradiometer (MISR), MODerate-Resolution Imaging Spectroradiometer (MODIS) and Landsat Thematic Mapper (TM) data (Comar et al. 2014). The AVHRR, MISR and MODIS sensors have a large width and wide field of view. Due to this, they are able to receive adequate data within a relatively short period and can subsequently retrieve the BRDF with semiempirical models successfully. However, the wide coverage and low spatial resolution of these sensors may lead to mixed surface pixels. The TM sensor has a high spatial resolution that is able to better reflect surface details. However, it is not suitable for a wide range of real-time surface BRDF inversions because of its narrow width, low temporal resolution and single angle. The Chinese satellite HJ-1 has several advantages for BRDF quantitative inversion, including its wide width, high spatial resolution and high temporal resolution. To date, few studies have demonstrated short time retrievals of multi-angular data of each pixel in HJ-1/charge-coupled device (CCD) images. Therefore, it is important to explore the surface BRDF model of the HJ-1 satellite, because it can further the development of quantitative remote sensing and satellite data applications.

Data and study area

Satellite data

The HJ-1A/B satellite was launched on September 6, 2008. The CCD data of the HJ-1A/B satellite have four bands with a spatial resolution of 30 m, time period of 4 days and a Universal Transverse Mercator (UTM) coordinate system. In this study, the HJ-1B/CCD (Table 1) is the data source and the subsequent CCD multi-angular reflectance is normalized using a semiempirical model. In addition to data quality considerations, we also took the satellite observation angles into account and tried to choose satellite data with large differences in observation angles to better reflect the anisotropy of surface reflections. Finally, we chose 4-day HJ-1B CCD data under clear sky conditions (July 30, 2012, August 3, 2012, August 5, 2012, and August 6, 2012) to get multi-angular observation data of each pixel to inverse the BRDF.

Study area

The study area is in Xilin Gol, Inner Mongolia, located at 43°24′ N, 116°48′ E. The area has a flat and homogeneous underlying surface (Fig. 1). It is located in a semiarid grassland climate with a cold and dry winter and a warm and moist summer. The area has steppe vegetation that includes goat grass, grass and forbs. A 15-day field spectroscopic observation experiment was performed, and multi-angular spectral observation data were collected. Figure 1 shows the experiment location.

Ground measurements

To check the precision of the BRDF inversion results, a series of grassland observation field experiments were conducted between 10:00 and 13:00, from July 30, 2012, to August 10, 2012 (N43° 26′ 26.5″, E116° 39′ 58.8″). The multi-angular characteristics of grassland BRDF were also surveyed. The surveyed grassland is a pristine semiarid landscape with sparse grass. A field-spec FR2500 spectrometer (ASD Inc., Boulder, CO, USA) was used to conduct the multi-angular observation experiments on cloud- and wind-free days. The top of the spectrometer was 2.0 m from the ground. The measurements were repeated twice for each viewing angle, and average values were calculated. We measured the reflectance spectrum of several solar zenith angles in the principle and perpendicular planes. The solar zenith angle is positive when viewing directions and incident directions are on the same side;

Table 1 Characteristics of HJ-1B/CCD

Channel	Spectrum (μm)	Spatial resolution (m)	Spectral types
1	0.43 ∼ 0.52	30	Blue
2	0.52 ∼ 0.60	30	Green
3	0.63 ∼ 0.69	30	Red
4	0.76 ∼ 0.90	30	Near-infrared

Fig. 1 Location of the study area
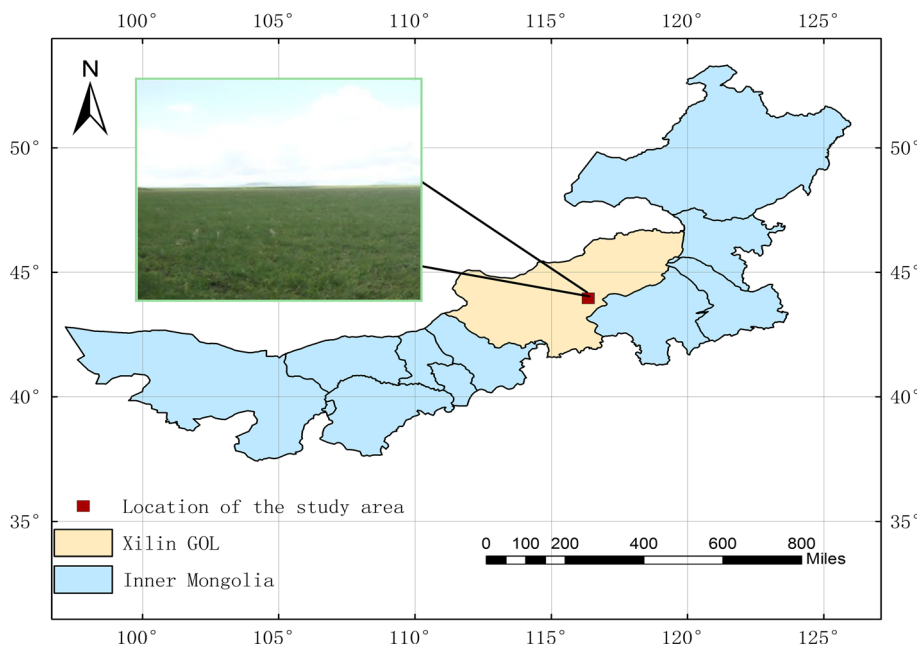
otherwise, it is negative. The view azimuth angle of 0° coincided with the north direction. The zenith angle was increased clockwise from 0° to 60° with a step size of 10°. Five lots of BRDF data in each survey area were obtained using a reference plate before and after each lot of grassland measurements.

Methodology

Figure 2 describes the stepwise workflow.

First, we applied radiometric corrections to the multi-angular images based on radiometric calibration coefficients published by the China Centre for Resources Satellite Data and Application. Then, we created a look-up table based on the 6S model (Vermote et al. 1997) and applied an atmospheric correction based on the atmospheric correction parameters obtained from the look-up table. Finally, we calculated the inverted BRDF based on a kernel-driven Algorithm for Model Bidirectional Reflectance Anisotropies of the Land Surface (Ambrals) model and validated the results from a comparison with the measured BRDF.

Atmospheric correction

Assuming that the underlying surface is Lambertian, then the atmospheric apparent reflectance can be defined by Eq. (1):

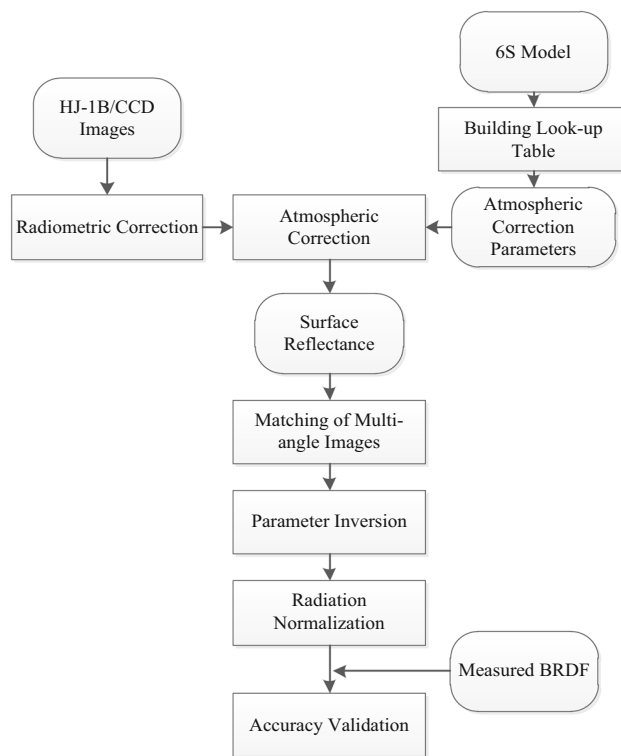$$\rho_{\text{TOA}}(\theta_s, \theta_v, \varphi_s - \varphi_v) = \pi \cdot L_\lambda d^2 / E_\lambda \cdot \cos(\theta_s) \qquad (1)$$

Fig. 2 Technical flow chart

where $\rho_{\text{TOA}}(\theta_s, \theta_v, \varphi_s - \varphi_v)$ represents the apparent reflectance of the λ-band, L_λ refers to the apparent radiance of the λ-band, d is the Earth–Sun distance in astronomical units, and E_λ is the solar spectral irradiance of the λ-band in the upper atmosphere. This value can be calculated from the CCD data spectral response functions. θ_s, θ_v, φ_s, and φ_v

represent the solar zenith angle, view zenith angle, solar azimuth angle and view azimuth angle, respectively.

Equation (1) can be converted to the following equation (Lee and Kaufman 1986):

$$
\begin{aligned}
&\rho_s(\theta_s, \theta_v, \varphi_s - \varphi_v) \\
&= \frac{\rho_{TOA}(\theta_s, \theta_v, \varphi_s - \varphi_v) - \rho_0(\theta_s, \theta_v, \varphi_s - \varphi_v)}{T(\theta_s)T(\theta_v) + (\rho_{TOA}(\theta_s, \theta_v, \varphi_s - \varphi_v) - \rho_0(\theta_s, \theta_v, \varphi_s - \varphi_v))S}
\end{aligned}
\tag{2}
$$

where ρ_s is the reflectance of the land surface and S, ρ_0, $T(\theta_s)$ and $T(\theta_v)$ are four necessary atmospheric correction parameters. $T(\theta_s)T(\theta_v)$ will be replaced by T in subsequent formulas. Equation (2) shows that the atmospheric correction needs three atmospheric correction parameters: S, ρ_0, T. It is difficult to obtain target atmospheric correction parameters by solving the radiative transfer equation; thus, the look-up table method is commonly used (Liu 2010).

Atmospheric correction methods based on radiative transfer models are very accurate. There are several such models, including the 6S (Second Simulation of the Satellite Signal in the Solar Spectrum) (Vermote et al. 1997), LOWTRAN (Wu 1998), MORTRAN (Wang et al. 2002), ATCOR (Matthew et al. 2002), UVRAD, ATREM and TURNER (6S User Guide version 2 1997). In this study, we develop a look-up table through the implementation of the 6S model and by assuming that the underlying surface is Lambertian and homogeneous. The 6S model has been extensively implemented and validated (Zhao 2003). Many radiative transfer codes have been documented and are known within the remote sensing community. The 6S model calculates scattering and absorption by integrating the method of latest approximation and a successive order of scattering. This work is built on the 5S model and is able to achieve inversion results much closer to actual values (Strahler et al. 1999). The atmospheric correction of CCD data from the HJ-1B satellite was implemented for each pixel from the look-up table. Due to the differences in the spectral response functions at each of the four bands of the CCD data, the look-up table was used for each band. Changes in aerosol optical depth, solar zenith angle, satellite zenith angle and other parameters are typically taken into account during atmospheric corrections, while the influence of water vapor is negligible and is thus not considered.

Four steps were needed to derive the atmospheric correction. First, a look-up table with atmospheric parameters S, ρ_0 and T was built. Second, the appropriate data from the look-up table were selected according to the bands, solar zenith angle, solar azimuth angle, viewing zenith angle and viewing azimuth angle of each pixel. Solar zenith angle and solar azimuth angle were obtained indirectly from the

header file. Satellite zenith angle and satellite azimuth angle were obtained from the downloaded Sat_Zenith_Azimuth.txt file. Third, different aerosol optical depths from the look-up table were used to interpolate the data to arrive at S, ρ_0 and T for each pixel. Aerosol optical depth was converted from the horizontal meteorological range. Finally, the atmospheric parameters of S, ρ_0 and T were substituted into Eq. (2) and combined with ρ_{TOA} to calculate surface reflectance. The utilized atmospheric model was mid-latitude summer and incorporated the rural aerosol mode. The solar zenith angles were set to 0°, 6°, 12°, 18°, 24°, 30°, 36°, 42°, 48°, 54°, 60° and 66°. The satellite zenith angles were 0°, 6°, 12°, 18°, 24°, 30°, 36°, 42°, 48°, 54°, 60° and 66°. The satellite azimuth angles were 0°, 12°, 24°, 36°, 48°, 60°, 72°, 84°, 96°, 108°, 120°, 132°, 144°, 156°, 168° and 180°. The aerosol parameter was set to continental. The aerosol optical depths at 550 nm were set to 0.0001, 0.25, 0.5, 1, 1.5 and 1.95. The altitude was 1276 m. These atmospheric parameters, in conjunction with the 6S model, helped build the look-up table. The atmospheric correction of the CCD data from the HJ-1B satellite was achieved using Interactive Data Language (IDL) programming.

Inversion algorithm of BRDF

There were four steps for BRDF inversion based on CCD data from the HJ-1B satellite: (1) collection and extraction of data sets in the same region as the four multi-angular images and subsequent calculation of the solar zenith angle, solar azimuth angle, view zenith angle, view azimuth angle and reflectance of each data set. (2) Matching of the multi-angular data sets, followed by extraction of the BRDF of each pixel from the matched data set. (3) Inversion of the parameters using semiempirical BRDF model according to the extracted BRDF for differing surface features. (4) Simulation of the normalized reflectance of the specified illumination-observing geometry, according to demand. This facilitated the comparison and analysis of remote sensing images between differing observation angles.

The BRDF model used in this study utilized a linear, kernel-driven Ambrals model, which depicts the directional reflection characteristics of the Earth's surface with a linear combination of kernels with certain physical meanings. The reflectances of mixed pixels were simulated by summing volume scattering, geometric scattering and isotropic scattering, as follows:

$$
\begin{aligned}
R(\theta_s, \varphi_s, \theta_v, \varphi_v) &= f_{iso} + f_{vol}K_{vol}(\theta_s, \varphi_s, \theta_v, \varphi_v) \\
&+ f_{geo}K_{geo}(\theta_s, \varphi_s, \theta_v, \varphi_v)
\end{aligned}
\tag{3}
$$

where R is the bidirectional reflectance, K_{vol} is the volume scattering kernel (Ross 1981), and K_{geo} is the geometric

scattering kernel (Li and Strahler 1992). All of the variables were functions of the viewing and incident directions. f_{iso}, f_{vol} and f_{geo} are parameters to be inversed and denote the weight of isotropic scattering, volume scattering and geometric scattering, respectively. We calculated the parameters f_{iso}, f_{vol} and f_{geo} by fitting the data with a linear regression model. The bidirectional reflectance of random incident direction and viewing direction was obtained by kernel extrapolation.

Ross–Thick Li–Sparse is a widely used kernel combination. Despite the algorithm's strong fitting capability, it loses physical meaning and can give negative reflectance values when zenith angles are large. To resolve this, Li Xiaowen proposed the Li–Transit kernel, to replace the Li–Sparse kernel with the Li–Dense kernel when zenith angles are large. The fitting capability of Li–Transit is similar to Li–Sparse, but the extrapolation capability of Li–Transit exceeds that of Li–Sparse (Strahler et al. 1999; Liu and Yang 2001). In this study, the Ross–Thick Li–Transit kernel combination was used to drive the Ambrals model. The Ross–Thick kernel was used to depict the volume scattering (Roujean et al. 1992; Ross 1981):

$$K_{\text{thick}} = \frac{(\pi/2 - \psi)\cos\psi + \sin\psi}{\cos\theta_s + \cos\theta_v} - \frac{\pi}{4} \tag{4}$$

where ψ denotes the scattering angle.

The Li–Transit kernel was used to depict the geometric scattering (Wanner et al. 1995):

$$K_{\text{Transit}} = \begin{cases} K_{\text{Sparse}} & B \leq 2 \\ K_{\text{Dense}} = \dfrac{2}{B} K_{\text{Sparse}} & \text{others} \end{cases} \tag{5}$$

$$K_{\text{sparse}} = O(\theta_i, \theta_r, \varphi) - \sec\theta_i' - \sec\theta_v' \\ + \frac{1}{2}(1 + \cos\zeta)\sec\theta_v'\sec\theta_i' \tag{6}$$
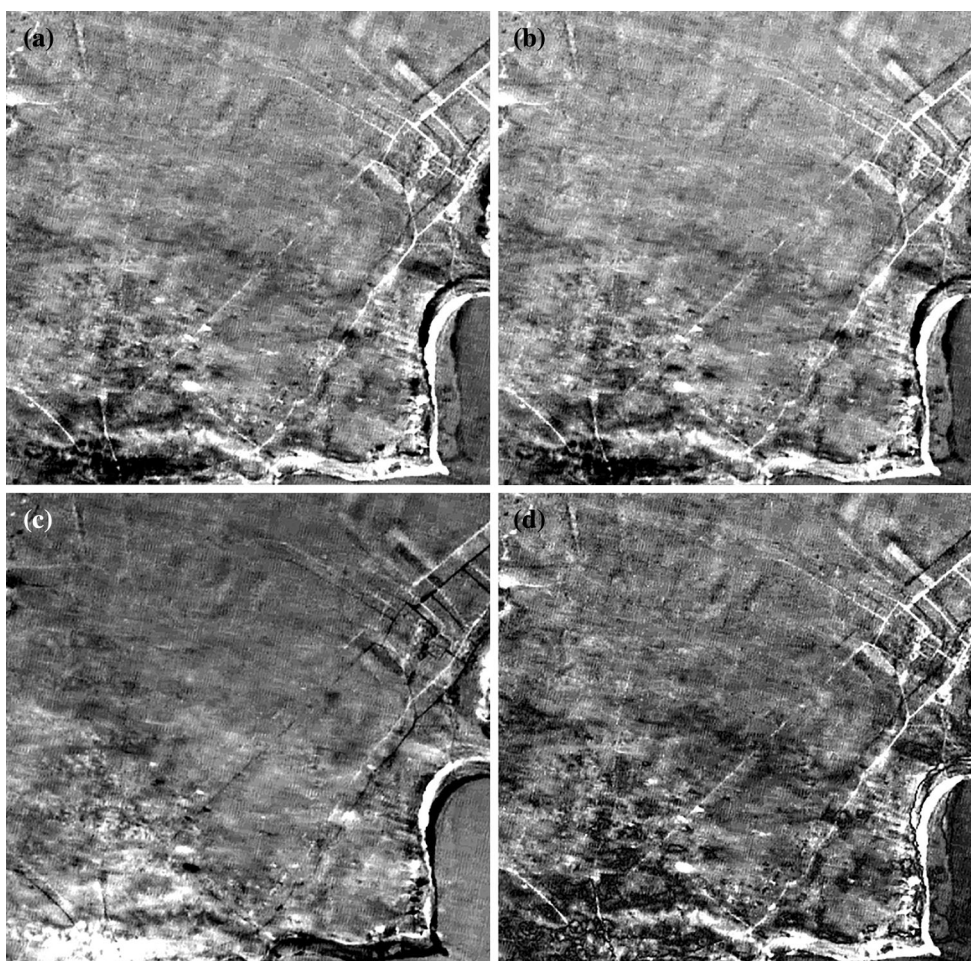
$$O(\theta_i, \theta_r, \varphi) = \frac{1}{\pi}(t - \sin t \cdot \cos t)(\sec\theta_i' + \sec\theta_v') \tag{7}$$

$$\cos t = \frac{h}{b} \frac{\sqrt{D^2(\tan\theta_i'\tan\theta_v'\sin\varphi)^2}}{\sec\theta_i' + \sec\theta_v'} \tag{8}$$

$$D = \sqrt{\tan^2\theta_i' + \tan^2\theta_v' - 2\tan\theta_i'\tan\theta_v'\cos\varphi} \tag{9}$$

$$\cos\zeta' = \cos\theta_i'\cos\theta_v' + \sin\theta_i'\sin\theta_v'\cos\varphi \tag{10}$$

Fig. 3 Inversion results of f_{iso} f_{geo} f_{vol} and BRDF. **a** Image of f_{iso}, **b** image of f_{geo}, **c** image of f_{vol}, **d** normalization of BRDF

$$\theta_i' = \tan^{-1}\left(\frac{b}{r}\tan\theta_i\right) \quad \theta_v' = \tan^{-1}\left(\frac{b}{r}\tan\theta_v\right) \quad (11)$$

where B is equal to 2 for continuity of the function and $O(\theta_i, \theta_r, \varphi)$ is the overlap area between the view and solar shadows. The term $\cos t$ was constrained to the range $[-1, 1]$; values outside of this range imply no overlap and should be disregarded. Note that the dimensionless crown relative height and shape parameters, $h = b$ and $b = r$, are within the kernel and should be preselected. For MODIS processing, as well as the examples given in this paper, $h = b = 2$ and $b = r = 1$, meaning that the spherical crowns were separated from the ground by half their diameter. Generally, the shapes of the crowns affect the BRDF more than their relative height (Wanner et al. 1995).

Results and analysis

Inversion results of BRDF model

The semiempirical kernel-driven Ambrals model was selected for BRDF inversion. The directional reflectance

can be normalized to specified angles under the requirements of users. Figure 3 displays the inversion results obtained using three parameters and normalized BRDF after implementation of the Ross–Thick Li–Transit kernel-driven model, based on HJ-1B/CCD data in the Inner Mongolia study area.

Comparison with measured BRDF

The expression of BRDF is primarily the linear expression of the geometrical optics scattering weight parameter and volume scattering weight parameter. The shape of the geometrical optics kernel (Li–Sparse kernel) is bow-like in the backscattering direction, and there is a hot spot peak. The shape of the volume scattering kernel (Ross–Thick kernel) is that of a bowl tilted slightly in the direction of forward scattering. Therefore, the simulated BRDF shapes based on different surface reflectances and measured data can be thought of as a composite of the two shapes (Zhang et al. 2015a, b).

Figure 4 is a comparison of measured and simulated grass BRDF from the kernel-driven model in the solar principle plane under equivalent geometric conditions
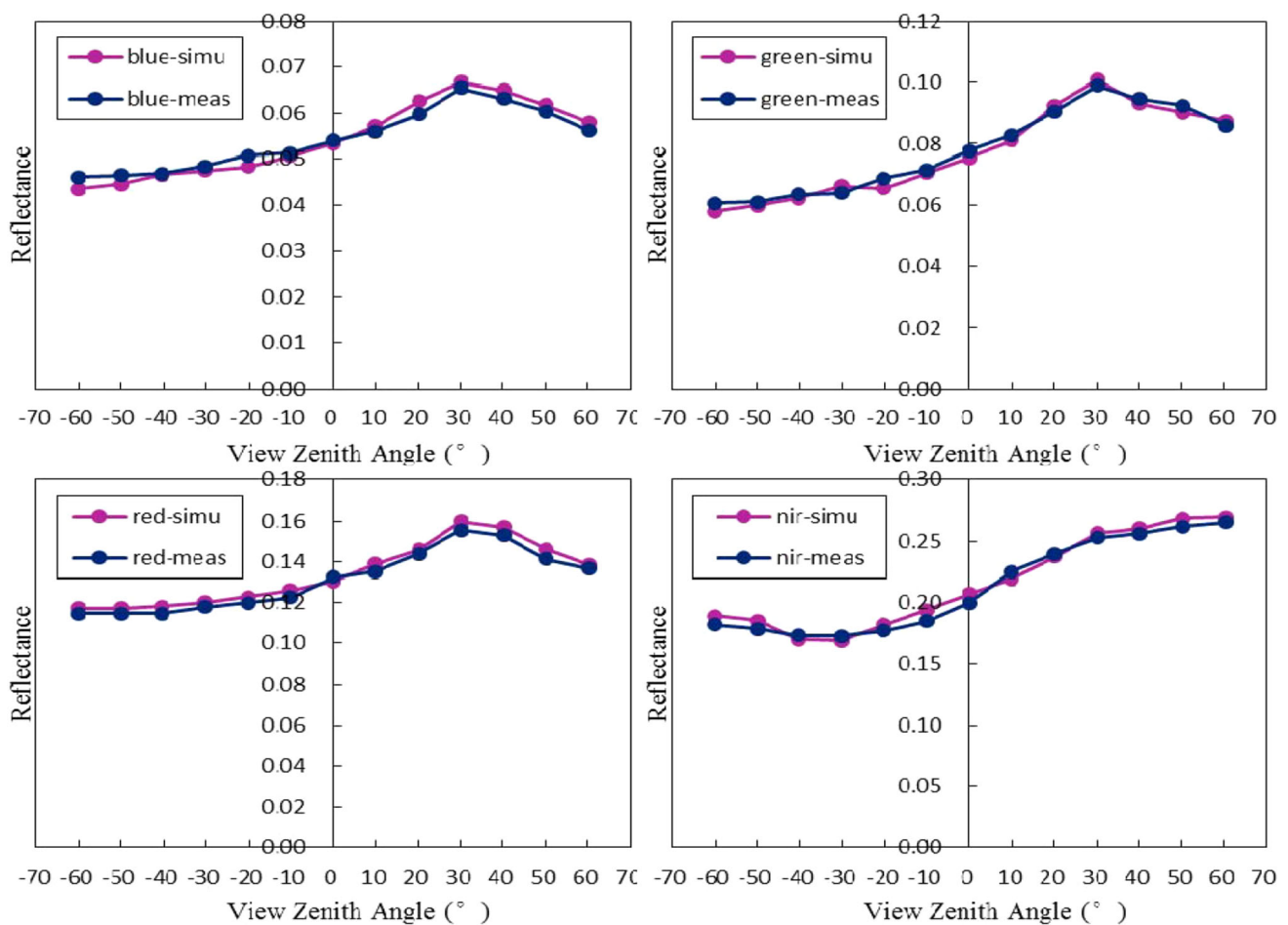

Fig. 4 Bidirectional reflectance *curves* of grass canopy in the principle plane of the Sun

(marked "meas" and "simu," respectively; solar zenith angle is 30°).

Figure 4 shows that the simulated BRDF values from the kernel-driven model agree well with the measured BRDF values in the blue, green, red and near-infrared bands under equivalent geometric conditions. This comparison demonstrates the following: (1) The bidirectional reflectance in the principle plane of the Sun has strong anisotropy, and bidirectional reflectance in the backward scattering direction is higher than that in the forward scattering direction. (2) Spectral curves of the visible band change dramatically, and there is a "hot spot" in the backward scattering direction at a zenith angle of 30°. (3) Due to multiple scattering, the bidirectional reflectance of the near-infrared band is minimally affected by angle. The bidirectional reflectance in the near-infrared band is high. The shape of the BRDF is bowl-like.

Figure 5 compares measured and kernel-driven model-simulated grass BRDFs in the perpendicular plane of the Sun under equivalent geometric conditions; they are marked "meas" and "simu," respectively.

Figure 5 shows that the simulated BRDF values from kernel-driven model agree well with the measured BRDF values in blue, green, red and near-infrared bands under the same geometric conditions. This comparison demonstrates the following: (1) The bidirectional reflectance in the principle plane of the Sun displays a weak anisotropy. The bidirectional reflectances in backward and forward scattering directions show symmetry. (2) The shape of the BRDF in the visible band is bow-like. The shape of the BRDF in the near-infrared band is bowl-like.

Accuracy validation

Relative error is typically used to compare and analyze the advantages and disadvantages of two or more methods. Relative error is calculated in the form of |V1−V2|/V2 (where V1 is the calculated value and V2 is the actual value) (Ross 1981). The relative error of measured and simulated BRDFs of grasslands is defined as:

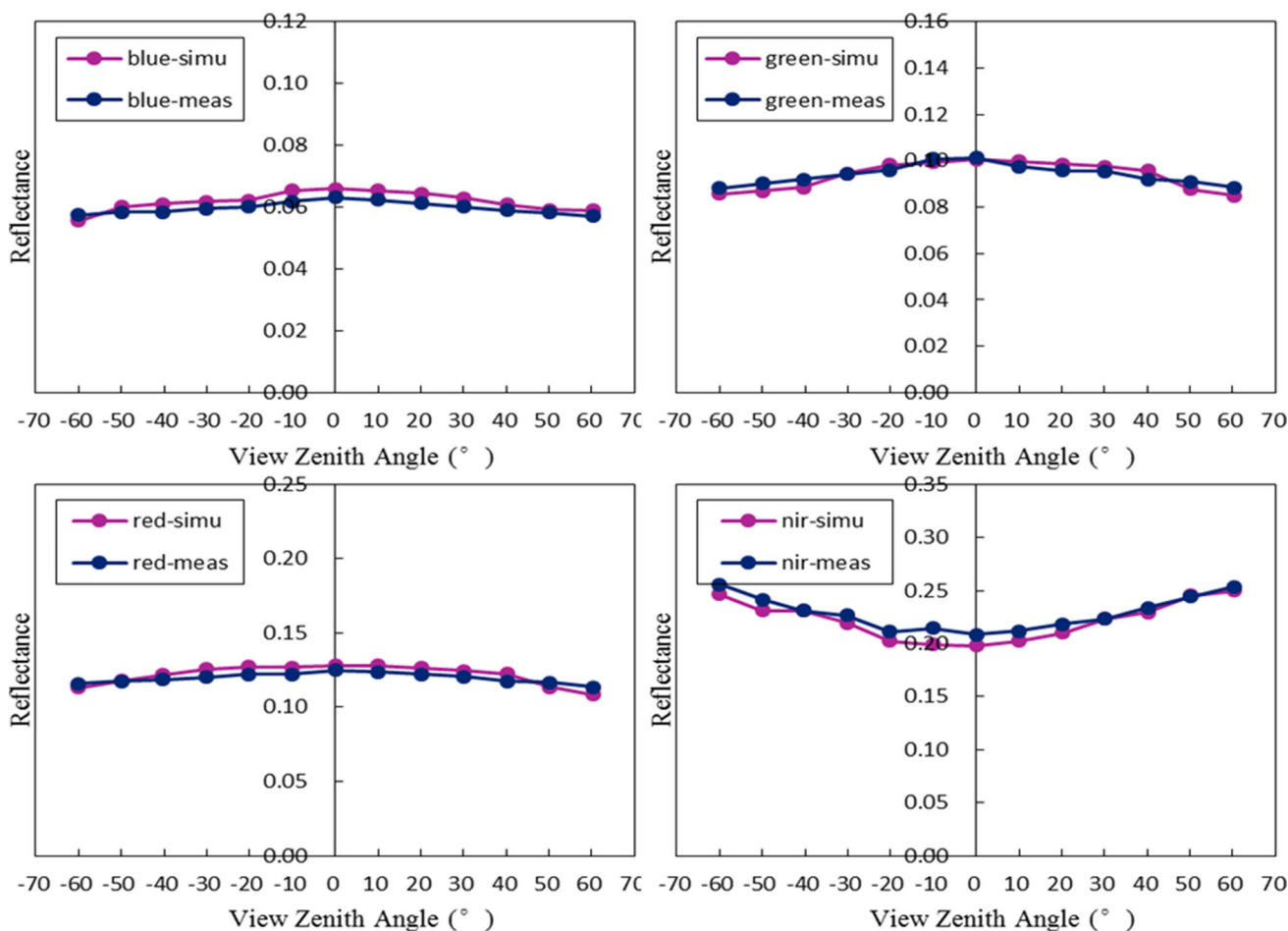$$e = \frac{|\rho_{simu} - \rho_{meas}|}{\rho_{meas}} \times 100\,\% \tag{12}$$

Fig. 5 Bidirectional reflectance *curves* of grass canopy in the perpendicular plane of the Sun

where e is relative error, ρ_{simu} is simulated BRDF on CCD data from the HJ-1B satellite, ρ_{meas} is measured BRDF, and "||" denotes absolute value.

1. Validation of BRDF in the principle plane of the Sun.

When verifying and evaluating the accuracy of simulated BRDF in the visible bands and near-infrared band with measured grassland data in the principle plane of the Sun, the viewing zenith angles were set to $-60°$, $-50°$, $-40°$, $-30°$, $-20°$, $0°$, $10°$, $20°$, $30°$, $40°$, $50°$ and $60°$. The results are shown in Fig. 6.

2. Validation of BRDF in the perpendicular plane of the Sun.

When verifying and evaluating the accuracy of simulated BRDF in the visible bands and the near-infrared band with measured grassland data in the perpendicular plane of the Sun, the viewing zenith angles were set to $-60°$, $-50°$, $-40°$, $-30°$, $-20°$, $0°$, $10°$, $20°$, $30°$, $40°$, $50°$ and $60°$; the results are shown in Fig. 7.
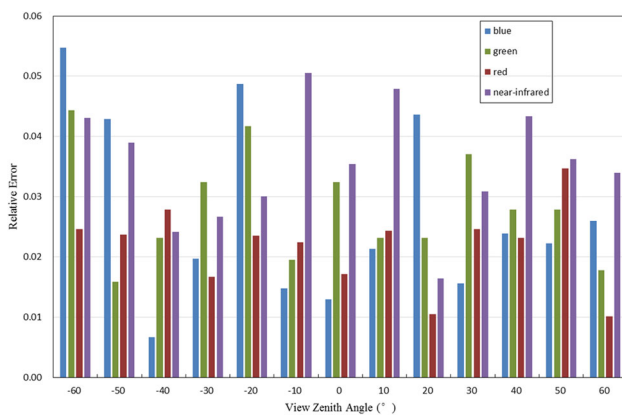

Fig. 6 Errors between measured BRDF and inversed BRDF in the principle plane of the Sun
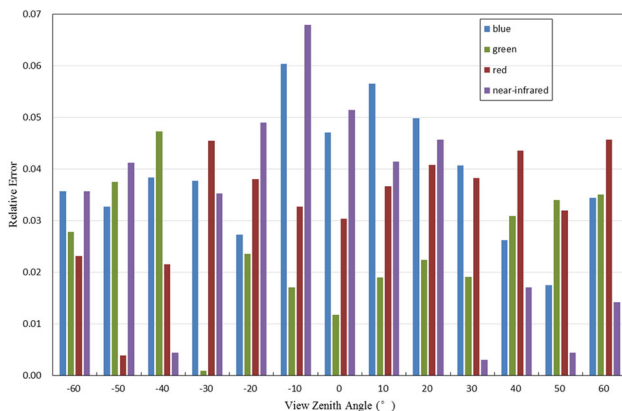

Fig. 7 Errors between measured BRDF and inversed BRDF in the perpendicular plane of the Sun

Figures 6 and 7 show that the errors in the visible bands and the near-infrared band in the principle plane of the Sun are within 6 %. The errors in the visible bands and the near-infrared band in the perpendicular plane of the Sun are within 7 %. Prior research has shown that the simulated surface reflectance can be considered valid when the relative error is <20 % (Sun 2011). In this regard, the BRDF inversion model presented in this study is valid and provides a reference for BRDF inversion calculation of uniform surfaces.

The principal sources of error are from the following: (1) error in the BRDF inversion model. Ambrals is an older BRDF inversion model, but there are still some internal errors in the model. For example, the assumption of isotropic scattering and the choice of driving kernels can increase the model error. (2) Error in image processing. Prior to the BRDF inversion, we performed radiometric and atmospheric correction. This produced errors that were sent down the modeling chain. (3) Artificial error. The field measurements include human factors such as tilt of the reference plate. These can lead to measurement value errors and can create potential discrepancies between measured and simulated values.

Conclusions

To date, BRDF inversion studies have been based primarily on MODIS and TM data, while the study of BRDF inversion based on CCD data from the HJ-1 satellite is limited. Exploration of BRDF inversion based on CCD data from the HJ-1 satellite can further and improve applications of satellite data. On the assumption that underlying surface is homogeneous and Lambertian, we performed an atmospheric correction from the 6S radioactive transfer model with IDL scripts. We then performed inversion and normalization of BRDF by implementing a kernel-driven Ambrals model for grasslands based on CCD data from the HJ-1B satellite. The inversion results display high accuracies. The main conclusions and results are as follows:

1. The radiometric normalization of BRDF at different viewing and incident angles was realized based on CCD data from the HJ-1B satellite. The BRDF inversion was based on the Ambrals kernel-driven model and agrees well with the measured BRDF. The errors are within 7 %.
2. The bidirectional reflectance of grassland in the principle plane of the Sun displays a strong anisotropy. In the case of the Lambertian surface, bidirectional reflectance in a backward scattering direction is higher than that in a forward scattering direction. There is a

"hot spot" in the visible band when the viewing and incident directions are the same. There is no "hot spot" in the near-infrared band, because this band is not as affected by angle. The bidirectional reflectance in the principle plane of the Sun has weak anisotropy. The bidirectional reflectance in both the backward and forward scattering directions shows symmetry.

3. The BRDF curves are different between the visible and near-infrared bands based on CCD data from the HJ-1B satellite. The geometrical optics effect is a principal factor in the visible band, while the volume scattering effect is the principal factor in the near-infrared band.

Based on the above, we created not only an integrated atmospheric correction and an inversion of the BRDF process, but also the normalization of BRDF. The model inversion results display high accuracy. The research conducted in this study will provide a reference for BRDF inversion over complex terrain in the future.

References

Comar A, Baret F, Obein G, Simonot L, Meneveaux D, Vienot F, de Solan B (2014) ACT: a leaf BRDF model taking into account the azimuthal anisotropy of monocotyledonous leaf surface. Remote Sens Environ 143:112–121

Dickinson RE (1995) Land processes in climate models. Remote Sens Environ 51(1):27–38

Lee TY, Kaufman YJ (1986) Non- Lambertian effects on remote sensing of surface reflectance and vegetation index. IEEE Trans Geosci Remote Sens 24(5):699–708

Li XW, Strahler AH (1992) Geometrical-optical bidirectional reflectance modeling of the discrete crown vegetation canopy: effect of crown shape and mutual shadowing. IEEE Trans Geosci Remote Sens 30(2):276–292

Liu QY (2010) The atmospheric correction for visible-infrared region of HJ-1 constellation data. MSc. dissertation, Henan Polytechnic University

Liu J, Fan WY (2008) Review on BRDF model and the inversion strategy. Remote Sens Technol Appl 23(1):104–110

Liu Y, Yang Z (2001) MODIS remote sensing information processing theory and algorithm. Science Press, Beijing

Lofgren BM (1995) Surface albedo-climate feedback simulated using two-way coupling. J Clim 8(10):2543–2562

Matthew MW, Adler-Goden SM, Berk A, Felde G, Anderson GP, Gorodetzky D, Paswaters S, Shippert M (2002) Atmospheric correction of spectral imagery: evaluation of the FLAASH algorithm with AVIRIS data. Appl Imag Pattern Recogn Workshop 31(2):157–163

Rahman H, Pinty B, Verstraete MM (1993) Coupled surface-atmosphere reflectance (CSAR) model: 2. semiempirical surface model usable with NOAA advanced very high resolution radiometer data. J Geophys Res Atmos 98(D11):20791–20801

Ross J (1981) Tasks for vegetation sciences 3: the radiation regime and architecture of plant stands. Springer, Netherlands

Roujean JL, Leroy M, Deschamps PY (1992) A bidirectional reflectance model of the earth's surface for the correction of remote sensing data. J Geophys Res 97(D18):20455–20468

Strahler AH, Muller JP, MODIS Science Team Members (1999) MODIS BRDF/Albedo product: algorithm theoretical basis document version 5.0. eospso.nasa.gov

Sun Y (2011) A study on the grassland radiative dorsiventral and directional simulation and validation. Ph.D. dissertation, Institute of Remote Sensing Applications, Chinese Academy of Sciences

Vermote EF, Tanre D, Deuze JL, Herman M, Morcette JJ (1997) Second simulation of the satellite signal in the solar spectrum, 6S: an overview. IEEE Trans Geosci Remote Sens 35(3):675–686

Wang J, Pan J, Wang L (2002) An introduction to a spatially-adaptive fast atmospheric correction for satellite remote sensing images. Remote Sens Technol Appl 17(4):193–197

Wanner W, Li XW, Strahler AH (1995) On the derivation of kernels for kernel-driven models of bidirectional reflectance. J Geophys Res Atmos 100(D10):21077–21089

Wu BY (1998) Practical algorithm for atmospheric radiative transfer. Meteorological Press, Beijing

Zhang YC, Rossow WB, Lacis AA (1995) Calculation of surface and top of atmosphere radiative fluxes from physical quantities based on ISCCP datasets: method and sensitivity to input data uncertainties. J Geophys Res Atmos 100(D1):1149–1165

Zhang H, Jiao ZT, Dong YD, Li JY, Li XW (2015a) Albedo retrieved from BRDF archetype and surface directional reflectance. J Remote Sens 19(3):355–367

Zhang H, Jiao ZT, Dong YD (2015b) Evaluation of BRDF archetypes for representing surface reflectance anisotropy using MODIS BRDF data. Remote Sens 7(6):7826–7845

Zhao YS (2003) Remote sensing application analysis theory and method. Science Press, Beijing **S User Guide Version 2. 1997**